IPEM
Institute of Physics and
Engineering in Medicine

PAPER • OPEN ACCESS

On the robustness of multilateration of ionoacoustic signals for localization of the Bragg peak at pre-clinical proton beam energies in water

To cite this article: Ronaldo Kalunga *et al* 2023 *Phys. Med. Biol.* **68** 105010

View the article online for updates and enhancements.

You may also like

Physics in Medicine & Biology

IPEM
Institute of Physics and
Engineering in Medicine

CrossMark

OPEN ACCESS

PAPER

On the robustness of multilateration of ionoacoustic signals for localization of the Bragg peak at pre-clinical proton beam energies in water

Ronaldo Kalunga[1] , Hans-Peter Wieser[1] , Pratik Dash[1] , Matthias Würl[1] , Marco Riboldi[1] , Jörg Schreiber[1] , Walter Assmann, Katia Parodi[1,2,3,*] and Julie Lascaud[1,3]

[1] Department of Medical Physics, Ludwig-Maximilians-Universität München, Garching b. München, Germany
[2] German Cancer Consortium (DKTK), Partner Site Munich, Munich, Germany
[3] Both authors contributed equally.
[*] Author to whom any correspondence should be addressed.

E-mail: katia.parodi@physik.uni-muenchen.de

Keywords: ionoacoustics, thermoacoustics, range verification, proton therapy

Supplementary material for this article is available online

Abstract

Objectives. The energy deposited in a medium by a pulsed proton beam results in the emission of thermoacoustic waves, also called ionoacoustics (IA). The proton beam stopping position (Bragg peak) can be retrieved from a time-of-flight analysis (ToF) of IA signals acquired at different sensor locations (multilateration). This work aimed to assess the robustness of multilateration methods in proton beams at pre-clinical energies for the development of a small animal irradiator. *Approach.* The accuracy of multilateration performed using different algorithms; namely, time of arrival and time difference of arrival, was investigated *in-silico* for ideal point sources in the presence of realistic uncertainties on the ToF estimation and ionoacoustic signals generated by a 20 MeV pulsed proton beam stopped in a homogeneous water phantom. The localisation accuracy was further investigated experimentally based on two different measurements with pulsed monoenergetic proton beams at energies of 20 and 22 MeV. *Main results.* It was found that the localisation accuracy mainly depends on the position of the acoustic detectors relative to the proton beam due to spatial variation of the error on the ToF estimation. By optimally positioning the sensors to reduce the ToF error, the Bragg peak could be located *in-silico* with an accuracy better than 90 μm (2% error). Localisation errors going up to 1 mm were observed experimentally due to inaccurate knowledge of the sensor positions and noisy ionoacoustic signals. *Significance.* This study gives a first overview of the implementation of different multilateration methods for ionoacoustics-based Bragg peak localisation in two- and three-dimensions at pre-clinical energies. Different sources of uncertainty were investigated, and their impact on the localisation accuracy was quantified *in-silico* and experimentally.

1. Introduction

Owing to their characteristic inverse depth dose profile, proton beams deliver their maximal dose to tissue inside a confined volume (so-called Bragg peak, BP), offering better sparing of healthy tissues compared to other external beam therapies such as, electron or photon beam therapies (Newhauser and Zhang 2015, Baumann *et al* 2016). However, there are still physical and biological challenges in ion beam therapy limiting its full potential exploitation. One challenge is represented by range uncertainties which are, among others, present because of anatomical changes between the treatment fractions (Li *et al* 2015), inaccurate knowledge of the tissue stopping power relative to water, and patient misalignment (Andreo 2009, Paganetti 2012, Grün *et al* 2013, Knopf and Lomax 2013). Therefore, the possibility of *in vivo* range verification during proton therapy is expected to help

reducing the safety margins applied during the treatment (irradiated volume typically increased by 3% of the range along the beam axis) and hence decreasing the dose to the healthy tissues.
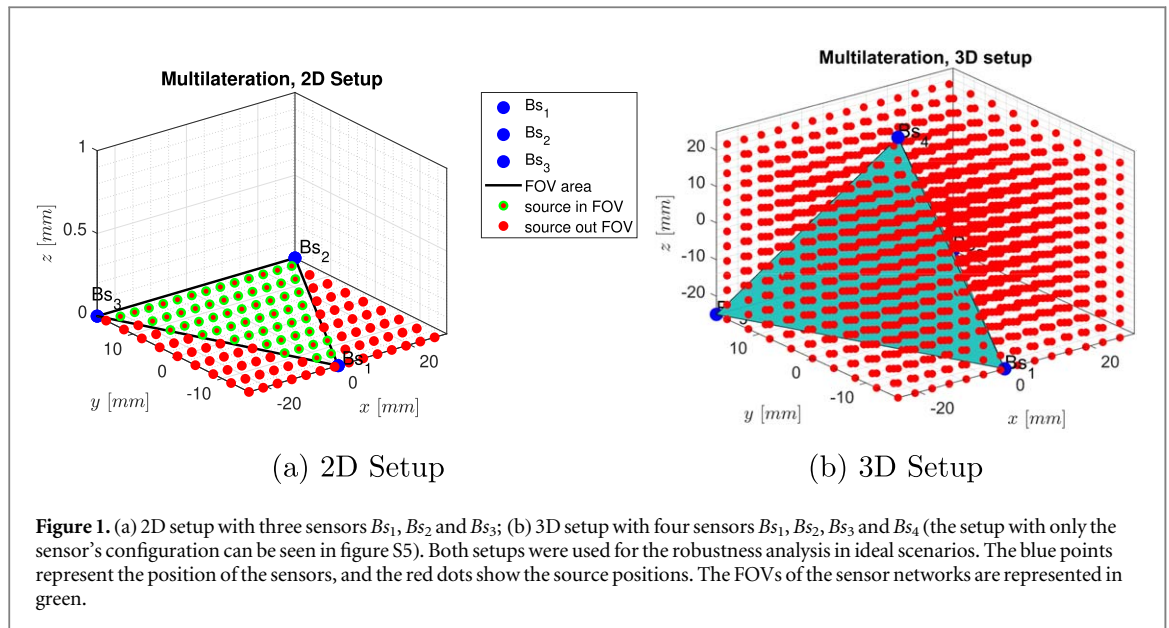
When energy is deposited in a medium by a pulsed proton or ion beam, it generates thermoacoustic waves, also called ionoacoustics (IA) (Jones *et al* 2014, Assmann *et al* 2015). Indeed, assuming sufficiently short proton pulses (thermal and stress confinement[4]), the irradiated volume briefly heats up due to the energy loss along the proton beam path, mostly caused by Coulomb inelastic interactions with the electrons in matter. The resulting initial pressure distribution is proportional to the deposited energy multiplied by a material-dependent conversion factor (Grüneisen parameter) (Hickling *et al* 2018). In homogeneous media, the acoustic emissions predominantly emerge from the BP volume allowing to retrieve the maximum of the deposited energy (or dose) from ToF estimation using acoustic localisation methods such as triangulation or multilateration. Alternatively, setting up a larger number of sensing elements, the full two- or three-dimensional dose can in principle be accurately reconstructed (Kellnberger *et al* 2016, Lascaud *et al* 2021b, Yao *et al* 2021) as the wave characteristics provide three-dimensional information on the underlying energy distribution.

In recent years, acoustic BP localisation based on linear least square approach (LS) using time of arrival (TOA) algorithm has been proposed as a method for range verification (Jones *et al* 2018, Patch *et al* 2018). These preliminary simulation studies have shown the first evidence of acoustic source localisation feasibility for *in vivo* range verification during prostate and liver irradiation. Acoustic BP localisation in a homogeneous medium based on nonlinear least square optimisation and the time difference of arrival (TDOA) algorithm has been proposed recently (Otero *et al* 2019). Contrary to TOA, which takes as inputs the ToFs estimated at each sensor position, TDOA relies on estimating the ToF difference between a reference sensor and all remaining sensors included in the network. Based on simulated and experimental data, the authors (Otero *et al* 2019) highlighted that the localisation accuracy depends on the number of sensors and their arrangement relative to the source position. In a complementary *in-silico* study from the same authors (Otero *et al* 2020), it was shown that BP could be located in the brain with an accuracy of 1mm. For all studies conducted by Otero and co-workers, the ToF was evaluated using generalized cross-correlation (Knapp and Carter 1976), but the effect of the ToF estimation method on the localisation accuracy was not discussed.

Since the ionoacoustic signal encodes information on the dose distribution, its temporal evolution (the signal shape) depends on the portion of the proton beam seen by a given acoustic sensor. Two main wavefronts are typically observed in homogeneous media (Jones *et al* 2016). A quasi-spherical wave propagating from the BP region (γ-wave) and a cylindrical wavefront (α-wave) from the plateau region. The energy variation at the position where the proton beam enters the phantom leads to the emission of an additional plane wave (entrance signal). The superposition of these different wavefronts results in a variation of the signal shape depending on the sensor position, which hampers accurate ToF estimation (Jones *et al* 2016). Other sources of uncertainties on the ToF determination in homogeneous media result from the detector response, the noise and an inaccurate knowledge on the measurement starting time (Lehrack *et al* 2017). In heterogeneous media, the variation of the speed of sound in the different tissues may cause additional errors in the ToF estimation if not properly taken into account (Jones *et al* 2018).

The present study investigates the robustness of BP localisation using TOA and TDOA multilateration algorithms at pre-clinical proton beam energies (20 and 22 MeV), in the context of the SIRMIO project (Parodi *et al* 2019). A compact portable system is developed along the SIRMIO project, allowing for precision image-guided small animal proton irradiation at existing clinical proton centres. The platform will include a dedicated beamline for degradation and refocusing of the clinical beam to relevant pre-clinical energies with sub-millimeter beam dimensions (Gerlach *et al* 2020). The anatomical images will rely on proton computed tomography of the animal in the treatment position before irradiation (Schnürle *et al* 2023), combined with ultrasound imaging for enhanced tumour visualisation. IA will be used for proton range verification with pulsed beams delivered by clinical synchro-cyclotron accelerators, to complement an in-beam positron emission tomography system foreseen for range monitoring at isochronous cyclotrons and synchrotrons, as well as for biological guidance. The compactness of the SIRMIO platform and co-integration of the different modalities limit the space available around the animal. Consequently, the number of IA sensors and their position should be optimised to not interfere with the treatment delivery and anatomical imaging, while allowing for accurate BP localisation. To this aim, the robustness of different localisation methods and sensor arrangements is assessed. The choice of the reference sensor for TDOA and the impact of the ToF uncertainties on the source localisation precision and accuracy are first estimated in ideal two- and three-dimensional scenarios. To this aim, the ToFs are geometrically derived from the Euclidean distances, and ToF errors are introduced. Thereafter, the accuracy of the ToF extracted from IA signals generated by a pulsed 20 MeV proton beam in water is assessed *in-silico* for

---

[4] The heating time is short enough to neglect the thermal diffusion in the irradiated volume and shorter than the time required for an acoustic wave to propagate across the heated volume.

Figure 1. (a) 2D setup with three sensors Bs_1, Bs_2 and Bs_3; (b) 3D setup with four sensors Bs_1, Bs_2, Bs_3 and Bs_4 (the setup with only the sensor's configuration can be seen in figure S5). Both setups were used for the robustness analysis in ideal scenarios. The blue points represent the position of the sensors, and the red dots show the source positions. The FOVs of the sensor networks are represented in green.

several ToF estimation methods and different sensor positions. Lastly, BP localisation is investigated experimentally for two different sensor arrangements and proton beam energies.
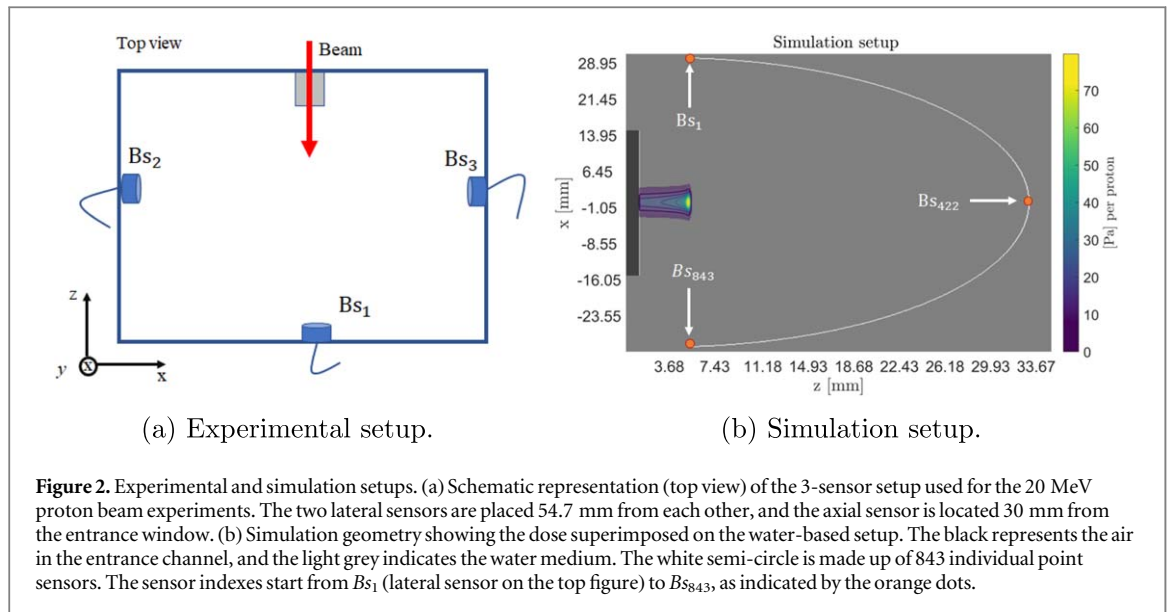
2. Material and methods

2.1. Simulation study

2.1.1. Robustness analysis in ideal scenarios

The geometries used to assess the influence of the ToF error on the multilateration outputs (robustness analysis) are illustrated in figure 1. Multilateration algorithms were first investigated in two-dimensions. An ideal source was virtually moved over 126 positions onto an orthogonal grid of 56×36 mm^2 by steps of 4 mm (see figure 1(a)). The ToFs were determined from the Euclidean distance between the source and the sensors, assuming a speed of sound of 1500 m s^{-1}. Here only 3 sensors (namely Bs_1, Bs_2 and Bs_3) were used, as illustrated in figure 1(a). The sensor positions were chosen based on the setup available for the ionoacoustic experiments described in section 2.2.1. The simulation geometry was later extended to three-dimensions, as shown in figure 1(b) (grid of $56 \times 36 \times 48$ mm^3 with a grid spacing of 4 mm), and a fourth sensor (Bs_4) was added on the top. To facilitate the result analysis, the field-of-view (FOV) of the sensor network is introduced and defined as the surface (or volume in 3D) enclosed by the sensors, as annotated in figure 1.

Random uncertainties in the ToF estimation were considered aiming to model speed of sound variations, inaccurate knowledge of the sensor's spatial location and error on the ToF. For that reason, the ToF error for each sensor was sampled from a multivariate normal distribution ($\mathcal{N}(\boldsymbol{\mu}, \boldsymbol{\Sigma})$) with mean zero and a standard deviation (σ_{random}) equal to 5% of the absolute ToF to reproduce *in vivo* variation of the speed of sound. There was no correlation between random uncertainties of individual sensors hence, off-diagonal elements in $\mathcal{N}(\boldsymbol{\mu}, \boldsymbol{\Sigma})$ were zero. Systematic uncertainties (i.e. coming from an inaccurate knowledge of the measurement starting time) were also considered and modelled by a multivariate Normal distribution. The standard deviation (σ_{syst}) was set to 1 μs according to previous studies from our group (Lehrack *et al* 2017, Wieser *et al* 2021). The systematic uncertainties on the ToF were assumed to be perfectly correlated between all the sensors (off-diagonal elements in $\mathcal{N}(\boldsymbol{\mu}, \boldsymbol{\Sigma})$ were >0). In the results presented hereafter, random and systematic uncertainties were modeled at the same time. The number of samples for each type of uncertainty was fixed to 150 ($N_{\mathrm{rand}} = 150$ and $N_{\mathrm{syst}} = 150$), which gives a total of 22 500 samples for each source position, chosen to have a representative sampling of the multilateration error distribution.

2.1.2. Ionoacoustic simulations

The performances of the multilateration algorithms (TOA and TDOA) for realistic ionoacoustic signals were evaluated *in-silico* in a homogeneous water phantom. The study's objective was to quantify the ToF error dependency on the sensor position. The three-dimensional dose distribution ($D(\mathbf{r})$) of a 20 MeV monoenergetic proton beam was obtained from the FLUKA Monte Carlo code (version 2020.0.4, using PRECISIOn defaults) (Ferrari *et al* 2005, Böhlen *et al* 2014). Additional information on the simulation setup can be found in the supporting material of Lascaud *et al* (2021a). The initial pressure ($p_0(\mathbf{r})$) was deduced from the deposited energy

Figure 2. Experimental and simulation setups. (a) Schematic representation (top view) of the 3-sensor setup used for the 20 MeV proton beam experiments. The two lateral sensors are placed 54.7 mm from each other, and the axial sensor is located 30 mm from the entrance window. (b) Simulation geometry showing the dose superimposed on the water-based setup. The black represents the air in the entrance channel, and the light grey indicates the water medium. The white semi-circle is made up of 843 individual point sensors. The sensor indexes start from Bs_1 (lateral sensor on the top figure) to Bs_{843}, as indicated by the orange dots.

($D(\mathbf{r}) \times \rho$, with ρ the water density equals to 998 kg m^{-3}) multiplied by the Grüneisen parameter (Γ=0.11). The initial pressure was propagated in three dimensions onto an anisotropic grid (spacing of 75 μm along the proton beam axis and lateral spacing of 150 μm) using the MATLAB k-Wave toolbox (MATLAB R2019a, MathWorks, Natick, MA) (Treeby and Cox 2010). Note that higher frequencies are propagated along the proton beam axis due to the sharpness of the BP (300 μm FWHM) compared to the lateral beam dimensions (2.5 mm FWHM at the phantom entrance was experimentally estimated from a Gafchromic film measurement), which motivated the choice of the anisotropic grid spacing. A 1 mm thick air gap positioned downstream to the proton beam was included in the k-Wave simulation setup, as illustrated in figure 2(b), to properly model the acoustic emission at the interface between the air and the water. The pressure waves were recorded using ideal point sensors (843 individual sensors) arranged in a semi-circular configuration with a diameter of 60 mm. The sensor network was positioned such that the center of the arc corresponds to the maximum of the proton dose. The arc dimension was chosen to be comparable with the setup used in the experiment shown in figure 2(a). After propagation, each signal was convolved with a 200 ns square pulse to account for the proton pulse shape observed experimentally.
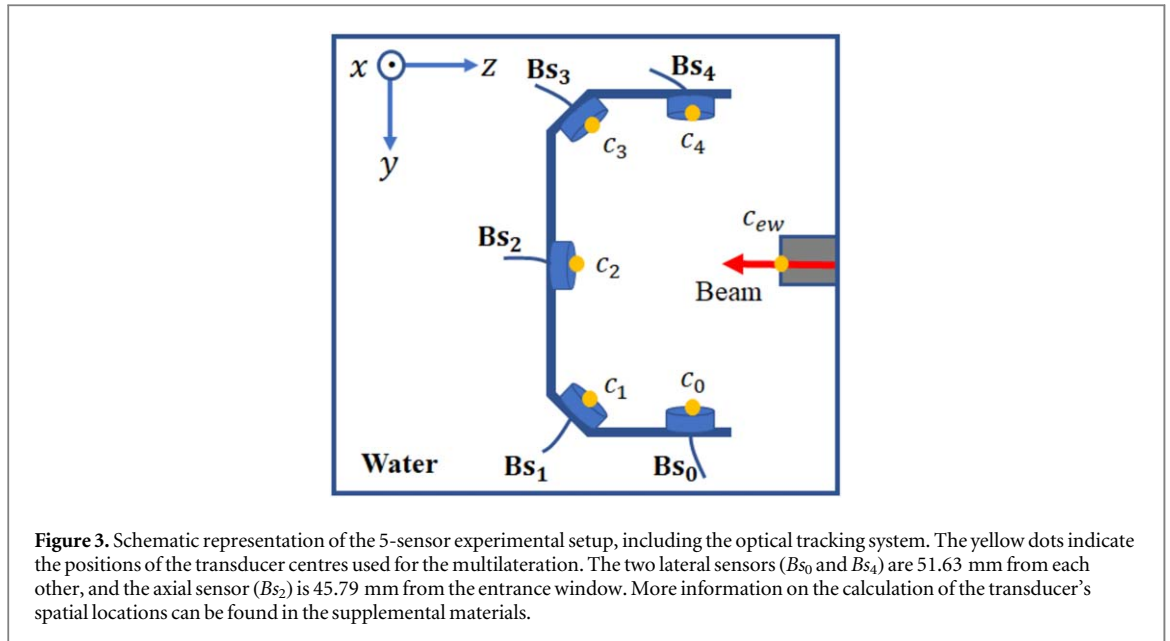
2.2. Ionoacoustic experiments

2.2.1. 3-sensor configuration

The experiment was conducted at the Maier-Leibnitz-Laboratory in Munich (Germany) with a 20 MeV monoenergetic pulsed proton beam in a water-filled aluminium box. For this first experiment, the beam was delivered by pulses of 200 ns at a repetition rate of 4.9 kHz. The beam current was set to 3 nA, corresponding to a dose per pulse of 1.69 Gy deposited at the BP. As illustrated in figure 2(a), the proton beam entered the setup by an air-channel terminated by a 50 μm thick polyimide foil (entrance window). The ionoacoustic wavefront was recorded using 3 detectors positioned on the proton beam axis (axial sensor) and on an axis perpendicularly to it (lateral sensors). The sensors were directly mounted into the aluminium box designed such that the BP was at the focus of all the detectors through water-sealed apertures in the wall, ensuring a fixed position of the detectors relative to the entrance window during the experiments. All the single element detectors were focused piezoelectric transducers manufactured by Olympus-Parametric (3.5 MHz centre frequency with a 73% fractional bandwidth and a diameter of 12.7 mm). The axial sensor Bs_1 had a focal length (fl) of 50.8 mm, whereas the focal length was equal to 25.4 mm for the two lateral detectors (Bs_2, Bs_3).

The setup was mounted onto a motorised three-axis stage used for alignment. To this purpose, ionoacoustic measurements were performed with the setup moved at different locations along the x- and y-axis (as defined on figure 2(a)) by steps of 1 mm. The setup was assumed to be aligned with the proton beam (hereafter referred to as the on-axis position) at the location for which the highest signal amplitude was detected on Bs_1. Additional measurements were performed after shifting by 5 mm the phantom along the x-axis (off-axis position).

The ionoacoustic signals were amplified by 60 dB using a low-noise amplifier (HVA-10M-60-B, FEMTO Messtechnik GmbH, Germany) before being acquired with a digital oscilloscope (6404D PicoScope, Pico Technology Ltd., GB) at a sampling frequency of 156.25 MHz. The signal acquisition was triggered using a synchronisation signal delivered by the chopping system of the particle accelerator. Such a trigger results in a time offset of 1.43 μs between the starting time of the measurement and the time at which the first protons hit the target, as previously characterised (Wieser *et al* 2021), which was later subtracted to the estimated ToF. The

Figure 3. Schematic representation of the 5-sensor experimental setup, including the optical tracking system. The yellow dots indicate the positions of the transducer centres used for the multilateration. The two lateral sensors (Bs_0 and Bs_4) are 51.63 mm from each other, and the axial sensor (Bs_2) is 45.79 mm from the entrance window. More information on the calculation of the transducer's spatial locations can be found in the supplemental materials.

measurements were systematically composed of 1000 consecutive acquisitions (1000 proton pulses). The temperature was monitored during the experiment using a PT1000 probe immersed in the water. The mean temperature was found to be 21.92 °C, which corresponds to a speed of sound in water of 1488.1 ms^{-1}, later used to estimate the BP position from the signal ToF. For each acquisition, the signal was denoised in post-processing using the Daubechies wavelet family with 5 decomposition levels (Ayat *et al* 2009, Dautov and Özerdem 2018, Baldazzi *et al* 2020, Vallicelli *et al* 2021) and the BP was localised with a single shot (1.69 Gy).

2.2.2. 5-sensor setup
Additional experiments were performed in a water tank using a 5-sensor arrangement mechanically assembled together using a dedicated holder (*horseshoes*), as represented in figure 3. For this setup, the beam energy was increased to 22 MeV. The beam current was set to 3.5 nA at a repetition rate of 10 kHz, corresponding to a dose per pulse of 0.58 Gy delivered at the BP. Similarly to the previous experiments, 12.7 mm diameter piezoelectric single elements with a 3.5 MHz center frequency were used and arranged as follows: one axial transducer Bs_2 ($fl = 50.8$ mm), two transducers inclined by an angle of 28° w.r.t. the beam axis, i.e. Bs_1 and Bs_3 ($fl = 25.4$ mm), and two lateral transducers Bs_0 (unfocused) and Bs_4 ($fl = 25.4$ mm), as shown in figure 3. Due to the limited number of channels available on the picoScope, the ionoacoustic signals were acquired sequentially (first with Bs_0 to Bs_2, and second with Bs_2 to Bs_4). As earlier, the measurements were repeated over 1000 consecutive proton pulses. Due to the orientation of the transducers Bs_1 and Bs_3 with respect to the beam axis and lower dose per pulse, the signal-to-noise ratio (SNR) for the IA signals recorded by the two tilted transducers was lower compared to the previous experiments. Therefore, the signals were averaged over 50 acquisitions (total peak dose of 29 Gy deposited at the BP) before performing the wavelet filtering.

The spatial location of the transducers (c_0 to c_4) were estimated with a 3D optical tracking system (Hybrid Polaris Spectra System, Northern Digital Inc., Waterloo, ON, Canada) using a passive marker tool. For focused detectors, the sensor location was defined as the projection of the outer rim's centre onto the curved surface, as depicted in figure S9 of the supplementary material. To this aim, the position of the rim's center was estimated by locating 3 points on the circle, and its projection on the curved surface was retrieved from a fourth measurement on the curved surface. The transducer localisation's accuracy was improved by performing a 3D rigid registration (coherent point drift algorithm) between a template derived from the holder drawing (moving image) and the position obtained from the optical measurements. The position where the proton beam enters the water tank (location of the entrance window, c_{ew}) was determined by irradiating a Gafchromic film. The marked location of the irradiated area centre was later acquired with the optical tracking system.

2.3. Data analysis
2.3.1. Multilateration workflow
Figure 4 illustrates the multilateration workflow used for the BP localisation. The ToF was estimated for each sensor Bs_1 to Bs_n, where n is the number of sensors, located at a spatial location c_1 to c_j, respectively, and converted to a distance knowing the medium speed-of-sound (v_{medium}). Multilateration was performed afterwards either using TOA or TDOA algorithms. To this aim, the cost functions described in equations (1) and (2) for TOA and
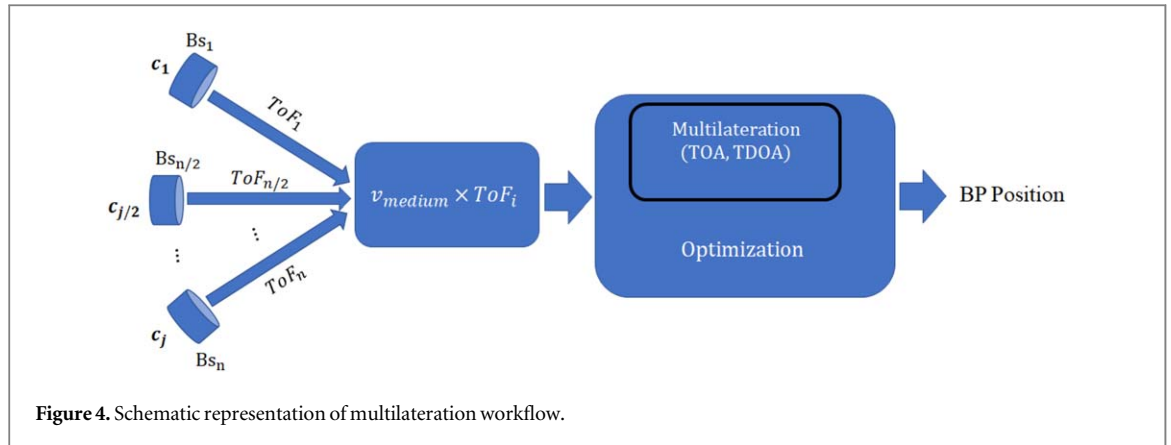
Figure 4. Schematic representation of multilateration workflow.

TDOA, respectively, were minimised using the Levenberg-Marquardt algorithm available from the Matlab software (Matlab R2021a) with 500 iterations and a termination tolerance set to 10^{-9}.

$$f_{\text{TOA}}(x_s, y_s, z_s) = \min_{x_s,y_s,z_s} \sum_{j=1}^{n} (v_{\text{medium}} \times \text{ToF}_j - \sqrt{(x_j - x_s)^2 + (y_j - y_s)^2 + (z_j - z_s)^2})^2 \quad (1)$$

$$f_{\text{TDOA}}(x_s, y_s, z_s) = \min_{x_s,y_s,z_s} \sum_{j=1}^{n} \sum_{\text{ref} \neq j} (v_{\text{medium}} \times \text{ToF}_j - \sqrt{(x_j - x_s)^2 + (y_j - y_s)^2 + (z_j - z_s)^2}$$

$$- v_{\text{medium}} \times \text{ToF}_{\text{ref}} + \sqrt{(x_{\text{ref}} - x_s)^2 + (y_{\text{ref}} - y_s)^2 + (z_{\text{ref}} - z_s)^2})^2. \quad (2)$$

Two types of reference sensors were considered for the study based on ideal scenarios (point sources at multiple locations) using TDOA, hereafter referred to as static or dynamic reference sensors. For the former, the same reference sensor is used independently of the source location, whereas for the latter, the reference sensor was changed depending on the ToF reads-out on each sensor of the network. Three dynamic allocation strategies were employed to define the reference sensor set, namely, the minimum ToF ($l^{\text{Ref,min}}$), the maximum ToF ($l^{\text{Ref,max}}$), or the average ToF ($l^{Ref,mean}$). For the latter, the reference sensor was selected to correspond with the detector for which the ToF is the closest (minimal difference) to the mean ToF across all the sensors.

2.3.2. Ionoacoustic time-of-flight extraction

For the studies with IA signals, the ToF was extracted from the direct signal (γ-wave), and different methods were compared. Figures 5(a) and (b) depict simulated IA signals recorded for different sensor positions (axial and lateral sensors, respectively) on which the several signal features used to extract the ToF are annotated. Those correspond to:
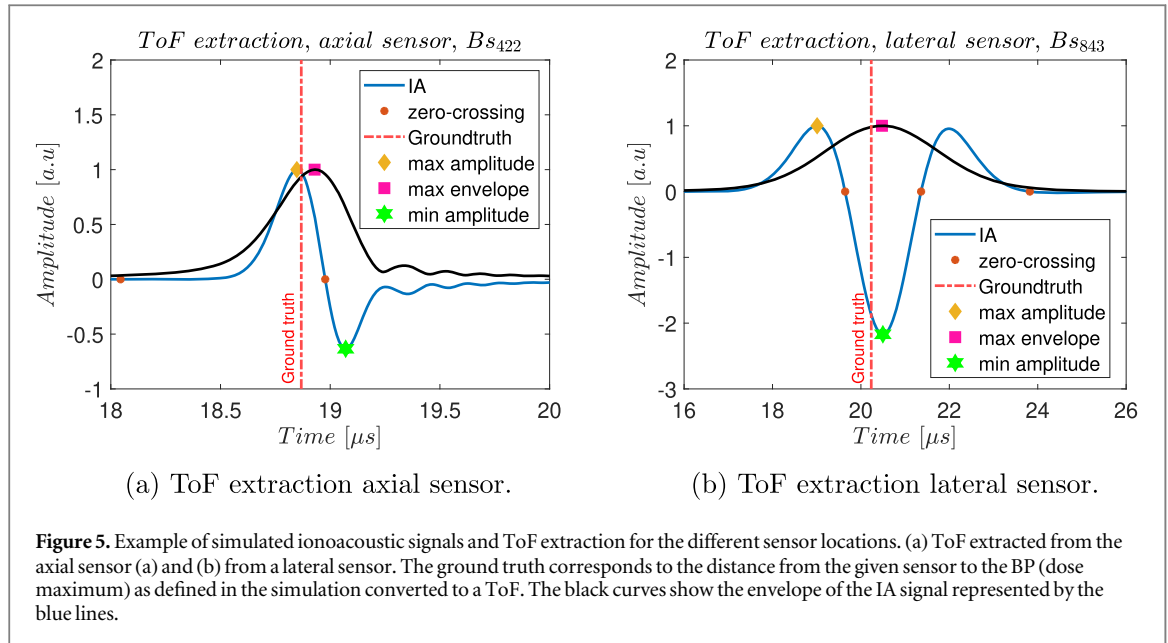
- The zero-crossing between the compression and rarefaction pulses for the axial sensor, hereafter referred to as zero-crossing. As seen in figure 5(b), for lateral sensors, there are multiple zero-crossing. In that case, the first zero-crossing point was chosen.

- The maximum of the signal amplitude (max amplitude).

- The minimum of the signal amplitude (min amplitude).

- The maximum of the signal envelope is obtained from the absolute value of the Hilbert transform (max envelope).

2.3.3. Multilateration robustness assessment

Without uncertainties, the accuracy was defined by the error in position, which is expressed as: $\epsilon_{xyz} = \sqrt{(x - x_s)^2 + (y - y_s)^2 + (z - z_s)^2}$. Where x, y and z are the known source positions and x_s, y_s, z_s are the reconstructed source position from the optimisation. The 3D metric is reducible to 1D (ϵ_z) or 2D (ϵ_{xz}) by cancelling the coordinate of the missing dimensions. For multiple source locations i.e. when the source position was moved, a mean value $\mu_{\epsilon_{xyz}}$ and a standard deviation $\sigma_{\epsilon_{xyz}}$ of the error in position were assessed. For the case of sources being inside the FOV, the corresponding error metrics are designated as $\epsilon_{xyz}^{\text{FOV}}$, $\mu_{\epsilon_{xyz}}^{\text{FOV}}$ and $\sigma_{\epsilon_{xyz}}^{\text{FOV}}$.

When uncertainties were modelled, the first metric was changed to be the root mean square error RMSE, i.e. the RMSE between the actual and estimated source position. From the RMSE other metrics were derived as, for instance, the mean root mean square error, i.e. μ_{RMSE}, and the standard deviation of the root mean square error,

Figure 5. Example of simulated ionoacoustic signals and ToF extraction for the different sensor locations. (a) ToF extracted from the axial sensor (a) and (b) from a lateral sensor. The ground truth corresponds to the distance from the given sensor to the BP (dose maximum) as defined in the simulation converted to a ToF. The black curves show the envelope of the IA signal represented by the blue lines.

i.e. σ_{RMSE}. Similarly, for the source located inside the sensor array FOV, the metrics were labelled as $\mathrm{RMSE}^{\mathrm{FOV}}$, $\mu_{\mathrm{RMSE}}^{\mathrm{FOV}}$ and $\sigma_{\mathrm{RMSE}}^{\mathrm{FOV}}$.

The accuracy of various ToF extraction methods was assessed by evaluating the error in ToF estimation, i.e. ϵ^{ToF}, which was defined as the product of the speed of sound in the medium, i.e. v_{medium}, and the absolute difference between the known ToF (ground truth) and the ToF estimated for a particular extraction method. For all the results reported afterwards, the ground truth for the 20 and 22 MeV proton beam were determined from the corresponding FLUKA Monte Carlo simulations. Although the simulations were not compared to another independent measurement, the general good agreement obtained between the experimental and simulated IA signals gives confidence in the reliability of the model used, which was also previously validated in a time-of-flight spectrometry study (Würl *et al* 2018). Moreover, for the experimental studies the SNR for each single sensor position, was defined as the ratio between the peak-to-peak amplitude and the noise standard deviation, defined as: $\mathrm{SNR}^{Bs_i} = \frac{V_{\mathrm{p-p}}[\mathrm{mV}]}{\sigma(\mathrm{Noise})[\mathrm{mV}]}$.
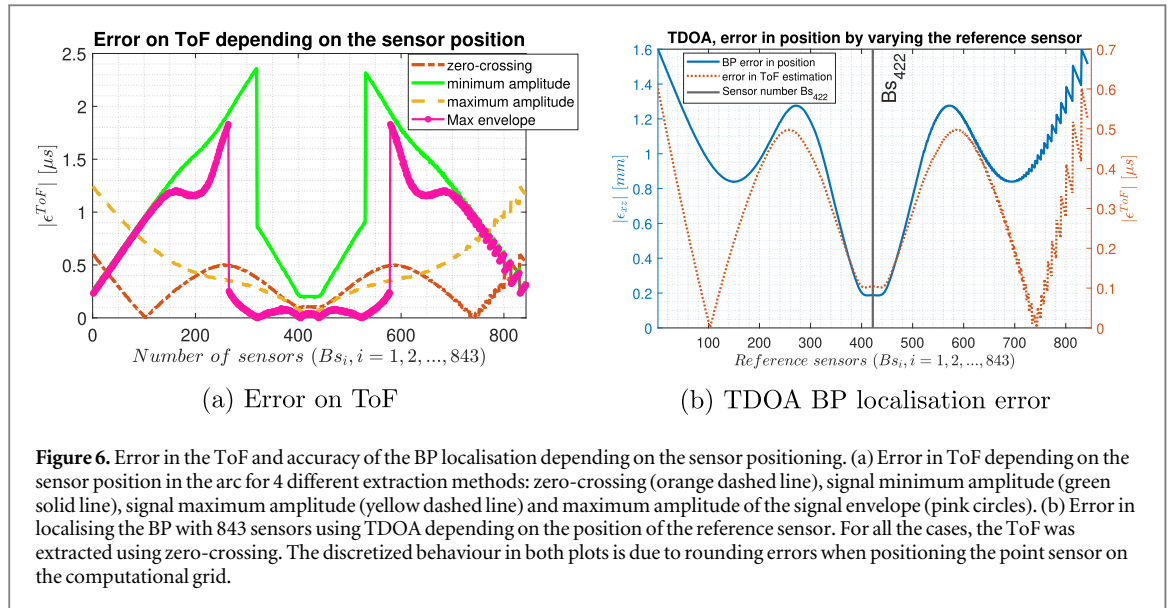
3. Results

3.1. Comparison between TOA and TDOA in 2D and 3D ideal scenarios

The performance of 2D multilateration in ideal scenarios was first assessed without uncertainties. In this case, the error obtained for TOA is almost independent of the source localisation and its position relative to the sensor network FOV (error of $\epsilon_{xy} = 0.81 \pm 0.46$ μm and $\epsilon_{xy}^{\mathrm{FOV}} = 0.74 \pm 0.59$ μm for all the sources position and restricting to the FOV, respectively (see figure S1)). Conversely, the error rapidly increases for sources outside the FOV when using TDOA and depends on the reference sensor. For the geometry investigated, the lowest errors are obtained using a static sensor (Bs_1) as a reference (error of $\epsilon_{xy} = 2.0 \pm 1.8$ μm and $\epsilon_{xy}^{\mathrm{FOV}} = 0.78 \pm 0.05$ μm, (see figure S1)). The corresponding mean errors and standard deviations are summarized in table 1.

Similarly to the previous results, with uncertainties the source localisation is more accurate at the center of the array independently of the method employed. For TOA, the error progressively increases inside the FOV when going from the center (RMSE of 1.63 mm) toward the edges (RMSE of 4.03 mm), leading to a $\mu_{\mathrm{RMSE}}^{\mathrm{FOV}}$ of 2.68 mm and a $\sigma_{\mathrm{RMSE}}^{\mathrm{FOV}}$ equals to 0.63 mm for the range of uncertainty modelled (see figure S4(a)). Using TDOA, the error is more homogeneous inside the FOV and slightly lower than for TOA at the center (RMSE = 1.61 mm). However, the error rapidly increases in the close vicinity of Bs_2 and Bs_3, going up to 4.03 mm for the sources closest to Bs_2. The mean root mean square error and its standard deviation were found to be $\mu_{\mathrm{RMSE}}^{\mathrm{FOV}} = 2.32$ mm and $\sigma_{\mathrm{RMSE}}^{\mathrm{FOV}} = 0.66$ mm (see figure S4(b)). The results for both algorithms are summarised in table S3.

For the multilateration performed in 3D, only the results in presence of random and systematic uncertainties are reported. For TOA, the mean root mean square error inside the FOV is equal to 3.74 mm with a standard deviation of 0.54 mm (see figure S8(a)). The mean error reduces when using TDOA ($\mu_{\mathrm{RMSE}}^{\mathrm{FOV}} = 3.35$ mm, whereas the standard deviation increases to 0.74 mm (see figure S8(b)). For both algorithms, as it was the case in 2D, the error increases when the source is located at the edges of the FOV with $\mathrm{RMSE}^{\mathrm{FOV}}$ going up to 5.35 mm and

(a) Error on ToF   (b) TDOA BP localisation error

Figure 6. Error in the ToF and accuracy of the BP localisation depending on the sensor positioning. (a) Error in ToF depending on the sensor position in the arc for 4 different extraction methods: zero-crossing (orange dashed line), signal minimum amplitude (green solid line), signal maximum amplitude (yellow dashed line) and maximum amplitude of the signal envelope (pink circles). (b) Error in localising the BP with 843 sensors using TDOA depending on the position of the reference sensor. For all the cases, the ToF was extracted using zero-crossing. The discretized behaviour in both plots is due to rounding errors when positioning the point sensor on the computational grid.

Table 1. Comparison of the performance of 2D multilateration using TOA and TDOA without uncertainties. TDOA is performed for different reference sensors such as: Bs_1, Bs_2, Bs_3, $l^{Ref,max}$, $l^{Ref,min}$, $l^{Ref,mean}$.

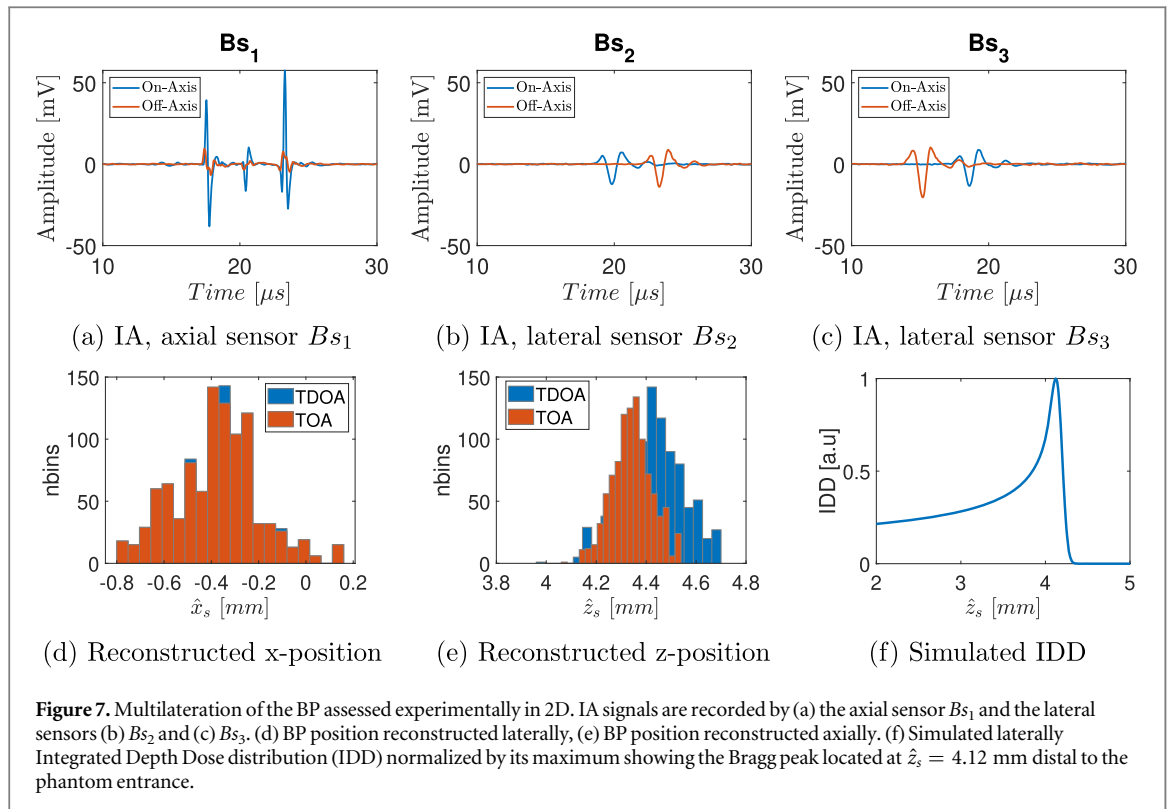| Multilateration methods	Reference sensor	$\mu_{\epsilon_{xy}}$ [mm]	$\mu_{\epsilon_{xy}}^{FOV}$ [mm]	$\sigma_{\epsilon_{xy}}$ [mm]	$\sigma_{\epsilon_{xy}}^{FOV}$ [mm]
TDOA	Bs_1	2.0×10^{-3}	7.8×10^{-4}	1.8×10^{-3}	4.8×10^{-5}
	Bs_2	2.4×10^{-3}	1.2×10^{-3}	2.0×10^{-3}	1.2×10^{-3}
	Bs_3	2.3×10^{-3}	1.1×10^{-3}	2.1×10^{-3}	8.9×10^{-4}
	$l^{Ref,max}$	1.9×10^{-3}	8.4×10^{-4}	1.5×10^{-3}	5.7×10^{-4}
	$l^{Ref,min}$	3.0×10^{-3}	1.5×10^{-3}	2.3×10^{-3}	1.3×10^{-3}
	$l^{Ref,mean}$	2.0×10^{-3}	6.9×10^{-3}	1.9×10^{-3}	3.8×10^{-3}
TOA	*none*	8.1×10^{-4}	7.4×10^{-4}	4.6×10^{-4}	5.9×10^{-4}

8.37 mm for TOA and TDOA, respectively. The lowest errors are observed at the centre where RMSE^{FOV} is as low as 2.58 mm and 2.47 mm for TOA and TDOA, respectively. All the results are reported in table S6.

3.2. Accuracy of ionoacoustic localisation depending on the sensor position

Figure 6(a) shows the error of the ToF determined from simulated ionoacoustic signals depending on the extraction method and for all the sensors (Bs_1 to Bs_{843}) in the arc array. For all the ToF extraction methods, the error in the ToF is minimum for axial sensors (Bs_{422}) and increases when going to lateral positions, i.e. Bs_1, Bs_{843}. The lowest errors are obtained by extracting the ToF from the signal *max envelope*, for which the error is lower than 0.1 μs at 4 positions near the beam axis (Bs_{322}, Bs_{403}, Bs_{441}, B_{523}). On average, for all the sensors positions investigated, the lowest error is obtained using *zero-crossing* method.

Figure 6(b) shows the performances of TDOA depending on the reference sensor, i.e. from Bs_1 to Bs_{843}, when the multilateration is carried out in 2D using all the 843 sensors of the array and extracting the ToF with the zero-crossing method. Similarly to the ToF error pattern, the localisation error is minimal for the reference sensor positioned on the beam axis ($\epsilon_{xz} = 0.18$ mm with Bs_{422} as a reference) and increases when selecting a lateral sensor as a reference (up to $\epsilon_{xz} = 1.60$ mm when Bs_1 is the reference). It is worth noticing that the minimum error on the ToF estimation (for Bs_{103} and Bs_{743}) does not correspond with the lowest localisation error.

Shown in table 2 are the errors in BP localisation using TOA and TDOA (with Bs_{422} as a reference) multilateration for various ToF extraction methods. Using 843 sensor positions, the ToF method resulting in the lowest error in the reconstructed BP position (error of 0.55 mm and 0.18 mm for TOA and TDOA, respectively) corresponds with those offering the lowest average ToF error (*zero-crossing*). Optimally selecting the sensors used for the multilateration and ToF extraction method to minimise the error on the ToF, the accuracy of the multilateration can be improved while decreasing the number of sensors required. For instance, using only 3 sensors (Bs_1, Bs_{422} and Bs_{843}) and evaluating the ToF from the maximum of amplitude of the signal envelope,

Figure 7. Multilateration of the BP assessed experimentally in 2D. IA signals are recorded by (a) the axial sensor Bs_1 and the lateral sensors (b) Bs_2 and (c) Bs_3. (d) BP position reconstructed laterally, (e) BP position reconstructed axially. (f) Simulated laterally Integrated Depth Dose distribution (IDD) normalized by its maximum showing the Bragg peak located at $\hat{z}_s = 4.12$ mm distal to the phantom entrance.

Table 2. Multilateration of the BP position in 2D for different ToF extraction methods. Two cases were considered, one for which all the 843 sensors were used, and a second, where only 3 sensors optimally selected were considered. The ground truth corresponds to the error on the multilateration when performed using a ToF derived from the Euclidean distance between the BP and the given sensors. For the multilateration performed with 843 sensors, the average error in ToF is also reported for all the sensor positions.

Number of sensors	ToF extraction	$\epsilon_{xz}^{\text{TOA}}$	$\epsilon_{xz}^{\text{TDOA}}$	Mean ϵ^{ToF}
843	Ground truth	0.15 μm	0.87 μm	
	Min amplitude	3.76 mm	1.19 mm	1.09 μs
	Max amplitude	0.62 mm	1.52 mm	0.50 μs
	Max envelope	4.49 mm	2.49 mm	0.64 μs
	Zero crossing	0.55 mm	0.18 mm	0.29 μs
3	Ground truth	2.00 μm	3.00 μm	
	Max envelope	0.09 mm	0.35 mm	0.19 μs

which allows for the lowest error for axial sensors, the localisation error reduces to 0.09 mm and 0.35 mm for TOA and TDOA with Bs_{422} as a reference, respectively.

3.3. Ionoacoustic experiments with 3 sensors

Figures 7(a) to (c) shows the IA signals recorded by the three detectors (axial sensor Bs_1 and the two lateral sensors Bs_2 and Bs_3) when the setup was positioned on the beam axis (on-axis) or after shifting it laterally by 5 mm (off-axis). As depicted on figure 7(a), the signal measured axially is made of three distinct pulses, namely the direct signal (from which the ToF was extracted), an entrance signal produced at the position where the proton beam enters the water phantom, and the reflection of the direct signal at the interface between air and water. As the energy gradients are sharper along the proton beam axis, the axial signal is of higher frequency and amplitude as the pressures measured laterally (figures 7(b) and (c) using Bs_2 and Bs_3, respectively). Considering the 5 mm shift, with regards to the 12.7 mm diameter of the transducers used, moving the setup laterally mostly affects the ToF derived from the lateral sensors (increased ToF from Bs_2 and reduced for Bs_3).

The distribution of the reconstructed lateral and axial locations of the BP for the 1000 consecutive measurements with the phantom positioned on the beam axis is presented in figures 7(d) and (e), respectively, in which both results obtained from TOA and TDOA are compared. The corresponding error on the BP position in

Table 3. Multilateration comparison TOA and TDOA *On-axis* and *Off-axis*. The BP was localised from single shot measurements (1.69 Gy). The reported localisation error corresponds to the mean value and standard deviation assessed from 1000 consecutive measurements.

Phantom position	Multilateration methods	Reference sensor	ToF extraction	$\epsilon_{\hat{z}_s}$ [mm]	$\epsilon_{\hat{x}_s\hat{z}_s}$ [mm]
On-axis	TOA	None	Max envelope	0.21 ± 0.08	0.43 ± 0.20
	TDOA	Bs_1	Max envelope	0.30 ± 0.12	0.48 ± 0.22
Off-axis	TOA	None	Max envelope	0.93 ± 0.07	1.26 ± 0.13
	TDOA	Bs_1	Max envelope	0.91 ± 0.09	1.25 ± 0.14

Table 4. SNR for single proton pulse measurements (1.69 Gy) acquired by the different sensors with the phantom *On-axis* and *Off-axis*. The SNR values were assessed from 1000 consecutive measurements, and correspond to the mean and standard deviation values.

Phantom Position	SNR^{Bs1}	SNR^{Bs2}	SNR^{Bs3}
On-axis	60.66 ± 3.41	19.08 ± 1.43	20.89 ± 1.38
Off-axis	14.91 ± 1.16	14.55 ± 0.73	26.81 ± 0.85

two dimensions is 0.43 ± 0.20 mm, and 0.48 ± 0.22 mm for TOA and TDOA (with Bs_1 as a reference sensor), respectively, as summarised in table 3. In both cases, the ToF was extracted using the signal *max envelope*, since it gives a lower ToF error for the lateral and axial sensors. The main contribution to the total error in position ($\epsilon_{\hat{x}_s\hat{z}_s}$) arises from the reconstruction of the lateral position ($\epsilon_{\hat{x}_s} = 0.37 \pm 0.17$ mm for TOA and TDOA, respectively), which is attributed to an inaccurate knowledge of the transducer position relative to the beam entrance (i.e. transducer location derived from the phantom center which was determined from a 1 mm step scan). With the phantom positioned off-axis, the total error in position increases to 1.26 ± 0.13 mm and 1.25 ± 0.14 mm for TOA and TDOA, respectively, resulting from inaccurate ToF estimation (i.e. the error on Bs_1 increases compared to the previous setup due to its almost lateral position) and lower SNR, as reported in table 4.

3.4. Ionoacoustic experiments with 5 sensors
Figures 8(a) and (b) show the results of BP multilateration in 3D performed with TOA and TDOA of the setup shown in figure 3. For this setup, for which particular attention was paid to the determination of the sensor locations, the total error on the determination of the 3D BP position reduces to 1.00 ± 0.72 mm and 0.82 ± 0.23 mm for TOA and TDOA, respectively. It is worth noticing that, without performing the proposed co-registration step to improve the accuracy of the sensor localisation, the BP multilateration error increases to 2.48 ± 0.30 mm for TOA and 8.82 ± 1.52 mm for TDOA.
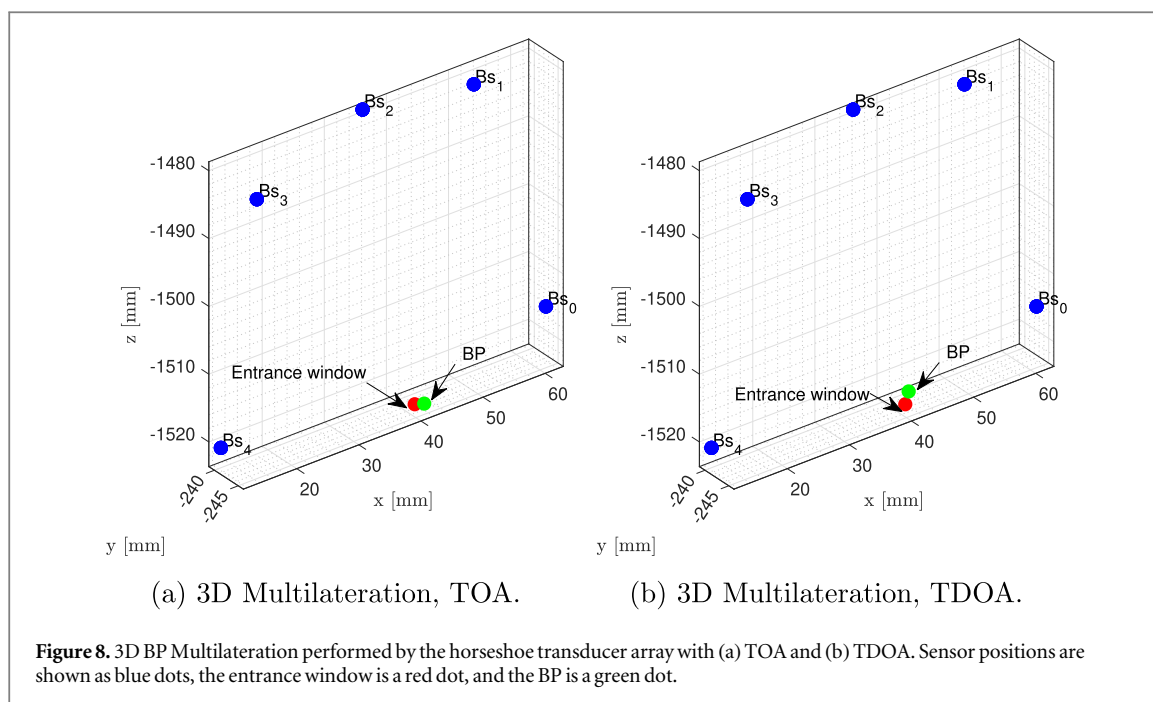
4. Discussion

4.1. TOA and TDOA algorithms in ideal scenarios
In an ideal scenario, i.e. without uncertainties, both TOA and TDOA perform similarly, although the accuracy of TDOA is more sensitive to the source location. Generally, the source should be inside the sensor array FOV, preferably in the centre. For the selected sensor geometry (36 mm height triangle) and range of uncertainties investigated, if the reference sensor is appropriately chosen, TDOA results in a lower localisation error ($\mu_{\text{RMSE}}^{\text{FOV}} = 2.32$ mm and $\mu_{\text{RMSE}}^{\text{FOV}} = 2.68$ mm for the TDOA and TOA, respectively) in presence of both random and systematic uncertainties. It should be noted that, TOA is more robust in presence of random uncertainties, with $\mu_{\text{RMSE}}^{\text{FOV}} = 2.19$ mm and $\sigma_{\text{RMSE}}^{\text{FOV}} = 0.41$ mm, compared to 2.32 ± 0.66 mm for TDOA (see information in the supplementary material). Conversely, if only considering systematic uncertainties, TDOA is more robust as the error cancels out ($\mu_{\text{RMSE}}^{\text{FOV}} = 7.8 \times 10^{-4}$ mm and $\sigma_{\text{RMSE}}^{\text{FOV}} = 4.8 \times 10^{-4}$ mm, going up to 1.03 ± 0.52 mm for TOA).

4.2. Starting time of the signal acquisition
For the experiments reported in this study, the measurements were triggered using a stable synchronisation signal provided by the chopping system of the tandem accelerator. The time difference between the rising edge of

Figure 8. 3D BP Multilateration performed by the horseshoe transducer array with (a) TOA and (b) TDOA. Sensor positions are shown as blue dots, the entrance window is a red dot, and the BP is a green dot.

the synchronisation signal and the actual moment when the protons enter the irradiated medium was previously determined with a precision better than 0.1 ns (corresponding to a distance smaller than 150 nm in water). The known offset on the acquisition starting time was thereafter systematically corrected during the data post-processing. By doing so, the systematic error is negligible compared to the error on the ToF estimation, and therefore, similarly to the simulations, the best results are obtained with TOA. Depending on the accelerator and facility, the access to a stable synchronisation signal directly from the machine may not be possible, as pointed out in a previous study for which a jittering of up to 850 ns was observed (1.3 mm in 22 °C water) at a clinical facility (Lehrack *et al* 2017). Alternatively, the acquisition can be triggered using an external detector to sense secondary emissions such as prompt gammas resulting from the interactions between the proton beam and the irradiated medium. In that case, the correlation between the triggering events and the proton pulse time profile should be known as it may introduce an additional time offset on the estimation of the ToF. All in all, if the relation between the synchronisation signal and the proton pulse cannot be determined or if the signal is not stable enough, multilateration using TDOA algorithm should be favoured.

4.3. Multilateration from ionoacoustic signals in homogeneous media

For ionoacoustic-based BP localisation in homogeneous medium of known speed of sound and assuming accurate knowledge of the sensor locations, the most relevant sources of uncertainties are the starting point of the measurement (systematic error on the determination of the exact time at which the first protons enter the irradiated phantom) and the error on the ToF extraction. As illustrated by the *in-silico* study with an arc sensor arrangement, the error on the ToF depends on the detector location relative to the BP. It is hence not correlated between all the sensors composing the array. Consequently, TOA provides more accurate BP localisation, which can be optimised by adequately selecting the sensor position to minimise the ToF error.

Moreover, as shown in the simulation studies, the performance of TDOA is intrinsically related to the choice of the reference sensor. In particular, for ionoacoustic applications, the error on the localisation can be up to 8 times higher depending on the reference sensor position and thus the error on the ToF estimation. However, the accuracy of the multilateration is not directly related to the ToF error observed on a given reference sensor (see figure 6(b)). The optimal reference sensor rather seems to correspond with positions for which the error on the ToF is close to the mean error, on average compensating for the ToF errors on the other sensors used for the multilateration.

4.4. Multilateration in heterogeneous media

The present study was limited to the irradiation of a homogeneous water phantom. In this case, the speed of sound in the medium is constant. However, the speed of sound varies *in vivo* depending on the tissue type, which is expected to reduce the BP localisation precision. Assuming a conservative 5 % error on the average speed of sound on the acoustic path, we showed that the error after multilateration increases by about 2 mm for the investigated geometry. Therefore, further implementation of multilateration for *in vivo* range verification

should account for the speed of sound aberration, similar to the strategy employed to track wireless capsule endoscopy using radio-frequency signals (Mohan *et al* 2016, Khan *et al* 2018). To this end, the speed of sound could be empirically derived from the x-ray pre-treatment imaging (Mast 2000) or imaged with ultrasound (Rau *et al* 2021) shortly before the treatment delivery. It is worth mentioning that a previous *in-silico* study has shown that the over- and under-estimation of the speed of sound along the propagation path tends to cancel out for the investigated clinical applications (liver and prostate). As a result, similar localisation errors were obtained for speed of sound assumed to be either the one in water or the correct average speed of sound estimated from x-ray images (Jones *et al* 2018).

4.5. Optimal sensor arrangement

Our results highlight the requirements for a preliminary study from the treatment plan (pre-treatment ionoacoustic simulation) to assess the ideal sensor position and reference sensor to mitigate the error on the ToF estimation. The adjustment of the sensor positioning should however be further studied, notably the robustness of the optimised arrangement when the BP is moved through the treatment field. In fact, as shown for the 3-sensor configuration experimentally investigated, similar localisation errors were obtained for TOA and TDOA when the proton beam was shifted by 5 mm laterally due to a larger error on the ToF. Therefore, the determination of the ideal sensor positions, their number and reference sensor for TDOA should be assessed for all the single beams composing the treatment plan (or at least for the ones with the highest intensity that are more reliable for the monitoring). Consequently, it also points out that a fixed sensor array geometry may not be optimal for multilateration, and sparse detector arrangement for which the sensor positions would be optimised for a given treatment plan will likely give the highest accuracy in localising the BP.

Furthermore, the sensor positioning should also consider the specific constraints of a given treatment plan. In particular, the locations where the beam enters the patient should be detector free to prevent the influence of the usually high-density, high-Z (atomic number) piezoelectric sensors on the beam quality and degradation of the IA detector performance. In the SIRMIO project, the small animal will be maintained in a sterile environment during the irradiation using a specially designed holder (Parodi *et al* 2019). The IA sensors should ideally be in direct contact with the animal skin to maximise the SNR of the detected signals. Therefore, the detectors should be positioned before enclosing the sterile space and setting it onto the SIRMIO platform. Bulky commercial ultrasonic detectors, as used in this study, cannot be inside the proton imaging FOV. Indeed, their large water equivalent thickness (WET $>>$ 1 cm) and atomic number Z would considerably increase proton scattering and consequently reduce the image resolution. This additional constraint further limits the locations where the IA detector can be positioned. As an alternative, sensors with a low material budget could be employed. Emerging ultrasonic transducer technologies such as micromachined transducers (Lascaud *et al* 2019) and optical hydrophones (Sueyasu *et al* 2022), or more conventional piezoelectric polymers with a dedicated acoustic design (Lascaud *et al* 2021c) that have been proposed in the recent years for ionoacoustics are possible candidates. However, further investigation is needed to determine whether such a sensor could be sensitive enough to detect the very low pressure of a few mPa (i.e. at least one order of magnitude lower than in clinical scenarios) expected in SIRMIO after degradation of the clinical proton beam (Lascaud *et al* 2022).

4.6. Transition to clinical applications

Assuming optimal synchronisation of the signal acquisition, proper speed of sound correction, and accurate positioning of the sensors, multilateration is fundamentally limited by the capability to extract the ToF. As illustrated by our results, the shape of the signal detected varies depending on the sensor position. This phenomenon is particularly enhanced at pre-clinical energies for which the proton range is relatively small compared to the propagation length and sensing aperture. In these conditions, the signals detected laterally are the superposition of the acoustic waves emerging from the BP, the plateau region, and potentially the energy discontinuity at the phantom entrance, which leads to a large error in the estimated ToF. Illustratively, for clinical applications, the proton range increases from about 4 mm at 20 MeV to 122 mm at 130 MeV in water, allowing for a better separation between the different wavefronts. The error on the ToF extraction for a setup similar to the one used in this study in the case of 130 MeV proton beam delivered at clinical synchrocyclotron accelerator is presented in figure S11b of the supporting material. The maximum error in the ToF is 0.75 μs, corresponding to a distance of 1.11 mm which is in good agreement with previous studies (Jones *et al* 2016, Lehrack *et al* 2017). This gives confidence that the knowledge gained at low proton beam energies can be applied to clinical scenarios.

It should be noted that the irradiation of a patient will give rise to additional acoustic emissions at the interfaces between the different tissues due to energy discontinuities and variation of the Grüneisen parameter. However, these signals of rather high spatial frequencies are expected to be filtered out when irradiating soft tissues by the microsecond proton pulse clinically available. Therefore, for favourable locations without bones or

air cavities in the acoustic and beam path, the millimetre accuracy seems achievable, as suggested by a recent experimental study in an anthropomorphic phantom (Patch *et al* 2021).

5. Conclusion

Acoustic localisation of the Bragg peak position in water was investigated *in-silico* and experimentally for pre-clinical scenarios. The robustness of two multilateration algorithms (TOA and TDOA) was compared, as well as the influence of the sensor position with respect to the proton beam on the localisation accuracy. The simulation study showed that the position of the Bragg peak in water could be located in two dimensions with an accuracy of 90 μm (2% error) when the sensors are optimally positioned to minimise the error on the time-of-flight estimation. Experimentally, the localisation error was found to vary between 0.4 mm to 1 mm depending on the sensor arrangement and beam energy, which was attributed to inaccurate knowledge of the sensor positions and/or intrinsic low signal-to-noise ratio resulting from the weak ionoacoustic emissions and their directivity. Further studies are required to assess the robustness of the multilateration method during the delivery of a (pre-) clinical treatment plan for which the moving position of the Bragg peak relative to the sensor array may result in a large variation of the acoustic localisation accuracy. Moreover, high doses were used during our experiments to improve the signal-to-noise ratio of the acquired ionoacoustic signals, this was done to investigate the method's performance under ideal statistical conditions, which could in future be achieved with improvements in detector technologies.

Acknowledgments

Data availability statement

All data that support the findings of this study are included within the article (and any supplementary information files). Data will be available from 31 March 2023.

ORCID iDs

Ronaldo Kalunga ⓘ https://orcid.org/0000-0003-4840-7187
Hans-Peter Wieser ⓘ https://orcid.org/0000-0002-2309-7963
Pratik Dash ⓘ https://orcid.org/0000-0001-9180-2065
Matthias Würl ⓘ https://orcid.org/0000-0003-3044-449X
Marco Riboldi ⓘ https://orcid.org/0000-0002-2431-4966
Jörg Schreiber ⓘ https://orcid.org/0000-0001-9904-9389
Katia Parodi ⓘ https://orcid.org/0000-0001-7779-6690
Julie Lascaud ⓘ https://orcid.org/0000-0002-7649-6909

References

Andreo P 2009 On the clinical spatial resolution achievable with protons and heavier charged particle radiotherapy beams *Phys. Med. Biol.* **54** N205–15
Assmann W *et al* 2015 Ionoacoustic characterization of the proton bragg peak with submillimeter accuracy *Med. Phys.* **42** 567–74
Ayat M, Shamsollahi M B, Mozaffari B and Kharabian S 2009 Ecg denoising using modulus maxima of wavelet transform *2009 Annual Int. Conf. of the IEEE Engineering in Medicine and Biology Society* (IEEE) pp 416–9
Baldazzi G, Solinas G, Del Valle J, Barbaro M, Micera S, Raffo L and Pani D 2020 Systematic analysis of wavelet denoising methods for neural signal processing *J. Neural Eng.* **17** 066016
Baumann M, Krause M, Overgaard J, Debus J, Bentzen S M, Daartz J, Richter C, Zips D and Bortfeld T 2016 Radiation oncology in the era of precision medicine *Nat. Rev. Cancer* **16** 234–49

Böhlen T, Cerutti F, Chin M, Fassò A, Ferrari A, Ortega P G, Mairani A, Sala P R, Smirnov G and Vlachoudis V 2014 The fluka code: developments and challenges for high energy and medical applications *Nucl. Data Sheets* **120** 211–4

Ferrari A, Ranft J, Sala P R and Fassò A 2005 *FLUKA: A multi-particle transport code (Program version 2005), number CERN-2005-10, Cern*

Gerlach S *et al* 2020 Beam characterization and feasibility study for a small animal irradiation platform at clinical proton therapy facilities *Phys. Med. Biol.* **65** 245045

Grün R, Friedrich T, Krämer M, Zink K, Durante M, Engenhart-Cabillic R and Scholz M 2013 Physical and biological factors determining the effective proton range *Med. Phys.* **40** 111716

Hickling S, Xiang L, Jones K C, Parodi K, Assmann W, Avery S, Hobson M and El Naqa I 2018 Ionizing radiation-induced acoustics for radiotherapy and diagnostic radiology applications *Med. Phys.* **45** e707–21

Jones K, Witztum A, Sehgal C and Avery S 2014 Proton beam characterization by proton-induced acoustic emission: simulation studies *Phys. Med. Biol.* **59** 6549

Jones K C, Nie W, Chu J C, Turian J V, Kassaee A, Sehgal C M and Avery S 2018 Acoustic-based proton range verification in heterogeneous tissue: simulation studies *Phys. Med. Biol.* **63** 025018

Jones K C, Seghal C M and Avery S 2016 How proton pulse characteristics influence protoacoustic determination of proton-beam range: simulation studies *Phys. Med. Biol.* **61** 2213

Jones K C, Vander Stappen F, Sehgal C M and Avery S 2016 Acoustic time-of-flight for proton range verification in water *Med. Phys.* **43** 5213–24

Kellnberger S, Assmann W, Lehrack S, Reinhardt S, Thirolf P, Queirós D, Sergiadis G, Dollinger G, Parodi K and Ntziachristos V 2016 Ionoacoustic tomography of the proton bragg peak in combination with ultrasound and optoacoustic imaging *Sci. Rep.* **6** 1–7

Khan U, Ye Y, Aisha A-U, Swar P and Pahlavan K 2018 Precision of em simulation based wireless location estimation in multi-sensor capsule endoscopy *IEEE J. Transl. Eng. Health Med.* **6** 1–11

Knapp C and Carter G 1976 The generalized correlation method for estimation of time delay *IEEE Trans. Acoust. Speech Signal Process.* **24** 320–7

Knopf A-C and Lomax A 2013 *In vivo* proton range verification: a review *Phys. Med. Biol.* **58** R131

Lascaud J, Kalunga R, Lehrack S, Wieser H-P, Englbrecht F S, Würl M, Assmann W, Savoia A S and Parodi K 2019 Applicability of capacitive micromachined ultrasonic transducers for the detection of proton-induced thermoacoustic waves *2019 IEEE Int. Ultrasonics Symposium (IUS)* (IEEE) pp 143–6

Lascaud J *et al* 2021a Enhancement of the ionoacoustic effect through ultrasound and photoacoustic contrast agents *Sci. Rep.* **11** 1–15

Lascaud J *et al* 2021b Investigating the accuracy of co-registered ionoacoustic and ultrasound images in pulsed proton beams *Phys. Med. Biol.* **66** 185007

Lascaud J *et al* 2021c Optimization of the backing material of a low frequency pvdf detector for ion beam monitoring during small animal proton irradiation *2021 IEEE Int. Ultrasonics Symp. (IUS)* (IEEE) pp 1–4

Lascaud J *et al* 2022 Fabrication and characterization of a multimodal 3d printed mouse phantom for ionoacoustic quality assurance in image-guided pre-clinical proton radiation research *Phys. Med. Biol.* **67** 205001

Lehrack S *et al* 2017 Submillimeter ionoacoustic range determination for protons in water at a clinical synchrocyclotron *Phys. Med. Biol.* **62** L20

Li H *et al* 2015 Robust optimization in intensity-modulated proton therapy to account for anatomy changes in lung cancer patients *Radiother. Oncol.* **114** 367–72

Mast T D 2000 Empirical relationships between acoustic parameters in human soft tissues *Acoust. Res. Lett. Online* **1** 37–42

Mohan A S, Boddupalli A, Hossain M D, Gozasht F and Ling S S 2016 Techniques for rf localization of wireless capsule endoscopy *2016 Int. Conf. on Electromagnetics in Advanced Applications (ICEAA)* (IEEE) pp 856–9

Newhauser W D and Zhang R 2015 The physics of proton therapy *Phys. Med. Biol.* **60** R155

Otero J, Felis I, Ardid M and Herrero A 2019 Acoustic localization of bragg peak proton beams for hadrontherapy monitoring *Sensors* **19** 1971

Otero J, Felis I, Herrero A, Merchán J A and Ardid M 2020 Bragg peak localization with piezoelectric sensors for proton therapy treatment *Sensors* **20** 2987

Dautov Ç P and Özerdem M S 2018 Wavelet transform and signal denoising using wavelet method *2018 26th Signal Processing and Communications Applications Conference (SIU)* (IEEE) pp 1–4

Paganetti H 2012 Range uncertainties in proton therapy and the role of monte carlo simulations *Phys. Med. Biol.* **57** R99

Parodi K *et al* 2019 Towards a novel small animal proton irradiation platform: the sirmio project *Acta Oncol.* **58** 1470–5

Patch S K, Hoff D E, Webb T B, Sobotka L G and Zhao T 2018 Two-stage ionoacoustic range verification leveraging monte carlo and acoustic simulations to stably account for tissue inhomogeneity and accelerator-specific time structure-a simulation study *Med. Phys.* **45** 783–93

Patch S K *et al* 2021 Thermoacoustic range verification during pencil beam delivery of a clinical plan to an abdominal imaging phantom *Radiother. Oncol.* **159** 224–30

Rau R, Schweizer D, Vishnevskiy V and Goksel O 2021 Speed-of-sound imaging using diverging waves *Int. J. Comput. Assist. Radiol. Surg.* **16** 1201–11

Schnürle K *et al* 2023 Development of integration mode proton imaging with a single cmos detector for a small animal irradiation platform *Front. Phys.* **10** 1384

Sueyasu S *et al* 2022 Ionoacoustic application of an optical hydrophone to detect proton beam range in water *Med. Phys.* **n/a** 1–12

Treeby B E and Cox B T 2010 k-Wave: MATLAB toolbox for the simulation and reconstruction of photoacoustic wave fields *J. Biomed. Opt.* **15**

Vallicelli E A, Corona M, Dell'Acqua M, Baschirotto A and De Matteis M 2021 Denoising for enhancing signal-to-noise ratio in proton sound detectors *2021 IEEE Biomedical Circuits and Systems Conference (BioCAS) (Berlin, Germany)* (Picastaway, NJ: IEEE) pp 1–4

Wieser H *et al* 2021 Experimental demonstration of accurate bragg peak localization with ionoacoustic tandem phase detection (itpd) *Phys. Med. Biol.* **66** 245020

Würl M *et al* 2018 Time-of-flight spectrometry of ultra-short, polyenergetic proton bunches *Rev. Sci. Instrum.* **89** 123302

Yao S, Hu Z, Xie Q, Yang Y and Peng H 2021 Further investigation of 3d dose verification in proton therapy utilizing acoustic signal, wavelet decomposition and machine learning *Biomed. Phys. Eng. Express* **8** 015008